Spectral Image Fusion From Compressive Measurements Using Spectral Unmixing and a Sparse Representation of Abundance Maps

Edwin Vargas, Henry Arguello, Jean-Yves Tourneret

Spectral Image Fusion From Compressive Measurements Using Spectral Unmixing and a Sparse Representation of Abundance Maps

Edwin Vargas, *Student Member, IEEE*, Henry Arguello, *Senior Member, IEEE*, and Jean-Yves Tourneret, *Fellow, IEEE*

***Abstract*— In the past years, one common way of enhancing the spatial resolution of a hyperspectral (HS) image has been to fuse it with complementary information coming from multispectral (MS) or panchromatic images. This paper proposes a new method for reconstructing a high-spatial, high-spectral image from measurements acquired after compressed sensing by multiple sensors of different spectral ranges and spatial resolutions, with specific attention to HS and MS compressed images. To solve this problem, we introduce a fusion model based on the linear spectral unmixing model classically used for HS images and investigate an optimization algorithm based on a block coordinate descent strategy. The nonnegative and sum-to-one constraints resulting from the intrinsic physical properties of abundances as well as a total variation penalization are used to regularize this ill-posed inverse problem. Simulation results conducted on realistic compressed HS and MS images show that the proposed algorithm can provide fusion results that are very close to those obtained with uncompressed images, with the advantage of using a significantly reduced number of measurements.**

***Index Terms*— Compressive sampling, data fusion, remote sensing, spectral imaging.**

I. Introduction

HYPERSPECTRAL (HS) sensors collect data that can be represented by a 3-D data cube [1]. This data cube referred to as HS image is a collection of 2-D images, each one captured at a specific wavelength. HS images are characterized by a high spectral resolution which allows accurate identification of the different materials contained in the scene of interest.

This work was supported by the Vicerrectoría de investigación y extensión, Universidad Industrial de Santander through "Sistema óptico-computacional para mejorar la resolución espacial de imágenes hiperespectrales usando técnicas de fusión a partir de datos obtenidos con esquemas de adquisición basados en muestreo compresivo" under Grant 2436 and under Grant ECOS Nord, intercambio de investi-gadores Colombia-Francia. Part of this work was also conducted within the STIC-AmSud Project HYPERMED. *(Corresponding author: Edwin Vargas.)*

E. Vargas is with the Department of Electrical Engineering, Universidad Industrial de Santander, Bucaramanga 680002, Colombia (e-mail: edwin.vargas4@correo.uis.edu.co).

H. Arguello is with the Department of Computer Science, Universidad Industrial de Santander, Bucaramanga 680002, Colombia.

J.-Y. Tourneret is with the IRIT/INP-ENSEEIHT/TéSA, University of Toulouse, 31071 Toulouse, France.

Color versions of one or more of the figures in this paper are available online at http://ieeexplore.ieee.org.

Digital Object Identifier 10.1109/TGRS.2019.2895822

Analyzing the spectral information of HS images has allowed the development of many applications in the fields of remote sensing [2], medical imaging [3], or astronomy [4]. However, due to technological reasons, HS images are limited by their relatively low spatial resolution [5]. For instance, the Hyperion imaging spectrometer has about 220 spectral bands, which extend from the visible region (0.4–0.7 μm) through the SWIR (about 2.5 μm), with a spatial resolution of 30 m by pixel [6] that can be insufficient for some practical applications.

In addition to their reduced spatial resolution, conventional spectral imaging devices have the drawback of requiring to scan a number of zones that grow linearly in proportion to the desired spatial or spectral resolutions. Finally, HS images require acquiring a large amount of data that must be stored and transmitted. To overcome these limitations, motivated by the compressed sensing (CS) theory [7], several compressive spectral imagers have been recently proposed [8]–[10]. Compressive spectral imaging (CSI) techniques [11], [12] exploit the fact that HS images are sparse in some basis and can be efficiently compressed by using CS. As a consequence, the images acquired with CSI have a reduced number of measurements when compared to conventional spectral imaging devices, which makes them attractive for many practical applications.

To overcome the spatial resolution limitation, a common trend is to fuse images with different spectral and spatial resolutions. A typical example studied in this paper is the fusion of HS images (having high spectral resolution) with multispectral (MS) images (having high spatial resolution) [13], [14]. Another example is HS pansharpening, which addresses the fusion of panchromatic and HS images [15]. Many algorithms have been proposed in the literature for image fusion (see [15], [16] for recent reviews). Fast fusion algorithms based on spectral mixture analysis have been developed to fuse HS and MS images [17], [18]. The coupled nonnegative matrix factorization has also been recently proposed to estimate the endmember and abundance matrices using an alternating optimization method [19].

This paper investigates a new algorithm allowing the fusion of HS and MS images acquired with compressive spectral imagers using a sparse representation of abundance maps.

The sparsity of abundance maps has already been exploited for image fusion. The compressive spectral fusion problem was recently investigated in [20] where the image of interest was decomposed in a fixed basis with a sparse representation. A related compressive fusion method based on a multiresolution analysis and a simple maximum selection fusion rule was previously proposed in [21], where the images to be fused were acquired in a single band with the same size. In this paper, we consider CSI devices such as the colored coded aperture snapshot spectral imager (C-CASSI) and the multiple snapshot spatial spectral coded compressive spectral imager (SSCSI), which sense multiple 2-D coded projections of the underlying scene. More formally, the projections measured in C-CASSI and SSCSI systems can be written as $\mathbf{y} = \mathbf{H}\mathbf{f}$, where $\mathbf{f} \in \mathbb{R}^{N^2 L}$ is a vector representation of the spatio–spectral 3-D source $\mathcal{F} \in \mathbb{R}^{N \times N \times L}$ ($N \times N$ is used for the spatial dimensions and L is the spectral dimension), and $\mathbf{H}$ is a matrix that is associated with the optical architecture of the spectral imagers. Note that the nonzero entries of $\mathbf{H}$ are determined by the colored coded aperture in the C-CASSI architecture [22] and by the coded mask in SSCSI [23]. Note also that these optical filters or coded apertures can be either randomly selected or designed as in [24] and [22], [25], [26].

The proposed fusion algorithm reconstructs the high-resolution (HR) image represented by the vector $\mathbf{f} \in \mathbb{R}^{N^2 L}$ from compressive measurements $\mathbf{y}_m$ and $\mathbf{y}_h$, resulting from MS and HS images associated with vectors $\mathbf{f}_m \in \mathbb{R}^{N^2 L_m}$ and $\mathbf{f}_h \in \mathbb{R}^{N_h^2 L}$. Note that the unknown image of interest is stacked into a column vector defined by $\mathbf{f} = [\mathbf{f}_1^T, \ldots, \mathbf{f}_L^T]^T \in \mathbb{R}^{N^2 L}$, where $\mathbf{f}_i \in \mathbb{R}^{N^2}$ contains all the image intensities associated with the ith spectral band. Furthermore, the target image has the high-spatial resolution of $\mathbf{f}_m$ and the high-spectral resolution of $\mathbf{f}_h$. The proposed algorithm is based on the linear mixture model (LMM), which assumes that each pixel of the target image is a linear mixture of spectral signatures (referred to as endmembers). Using the LMM, an observation pixel $\mathbf{f}_j \in \mathbb{R}^L$ can be represented as $\mathbf{f}_j = \mathbf{M}\boldsymbol{\alpha}_j$, where $\mathbf{M} \in \mathbb{R}^{L \times p}$ is the endmember matrix whose columns are spectral signatures, p is the number of materials in the image (supposed to be known) and $\boldsymbol{\alpha}_j = [\alpha_{j1}, \ldots, \alpha_{jp}]^T \in \mathbb{R}^p$ contains the abundances of the jth pixel of the HS image (see [27] for details). As a consequence, the target HS image can be written as $\mathbf{f} = \overline{\mathbf{M}}\boldsymbol{\alpha}$, where $\overline{\mathbf{M}} = \mathbf{M} \otimes \mathbf{I}_{N^2}, \mathbf{I}_{N^2} \in \mathbb{R}^{N^2 \times N^2}$ is the $N^2 \times N^2$ identity matrix, $\otimes$ is the Kronecker product, and $\boldsymbol{\alpha} = \text{vec}(\mathbf{A}^T) \in \mathbb{R}^{N^2 p}$ is obtained by vectorizing the matrix $\mathbf{A} = [\boldsymbol{\alpha}_1, \cdots, \boldsymbol{\alpha}_{N^2}] \in \mathbb{R}^{p \times N^2}$ containing the abundances of all the image pixels. The LMM was already used for image fusion in recent works such as [18] and [19]. However, these works did not take into account any CS operation (i.e., the matrices $\mathbf{H}_m$ and $\mathbf{H}_h$ were equal to the identity matrix), which is the main contribution of this paper.

This paper shows that acquiring images with CS and exploiting the LMM for the unknown image of interest and the sparsity of abundance maps leads to efficient image fusion when compared to existing approaches [18], [20], [21], even if the observed images have been compressed and acquired with reduced acquisition time. Note that the standard endmember extraction algorithms, such as vertex component analysis (VCA) [28], SVMAX [29], or N-FINDR [30], cannot be used directly when the observed images have been compressed. This endmember extraction step is contained within the proposed fusion algorithm.

The paper is organized as follows. Section II introduces the observation models used for the HS and MS images. The inverse problem considered for the proposed fusion method is also defined. Section III describes the principles behind CASSI and SSCSI used to sense spectral data. The optimization algorithm proposed to solve this inverse problem is presented in Section IV. Numerical results conducted on realistic HS and MS images are presented in Section V. A numerical analysis of the algorithm convergence is presented in Section VI. Conclusions and future work are reported in Section VII.

II. Problem Statement

This section formulates the data fusion problem considered in this paper to estimate a high-spatial / high-spectral resolution image from two compressed images with different spectral and spatial resolutions.

A. Observation Models

It is very common to assume that HS and MS images result from the application of linear spatial and linear spectral degradations to a higher resolution image $\mathbf{f} = \overline{\mathbf{M}}\boldsymbol{\alpha}$ [14], [18], [31]. Moreover, as we mentioned before, we propose to consider compressed spectral images that are modeled from linear projections. Thus, we consider the following models for the observed compressed MS and HS images

$$\begin{aligned} \mathbf{y}_m &= \mathbf{H}_m \mathbf{R}_\lambda \mathbf{f} + \mathbf{N}_m = \mathbf{H}_m \mathbf{R}_\lambda \overline{\mathbf{M}}\boldsymbol{\alpha} + \mathbf{N}_m \\ \mathbf{y}_h &= \mathbf{H}_h \mathbf{S}_\mathbf{s} \mathbf{f} + \mathbf{N}_h = \mathbf{H}_h \mathbf{S}_\mathbf{s} \overline{\mathbf{M}}\boldsymbol{\alpha} + \mathbf{N}_h \end{aligned} \tag{1}$$

where:

1) $\mathbf{R}_\lambda = \mathbf{R} \otimes \mathbf{I}_{N^2}$ models the linear spectral degradation, and $\mathbf{R} \in \mathbb{R}^{L_m \times L}$ is the spectral response of the MS sensor;
2) $\mathbf{S}_\mathbf{s} = \mathbf{I}_L \otimes \mathbf{S}\mathbf{B}$ models the spatial degradation, $\mathbf{B} \in \mathbb{R}^{N^2 \times N^2}$ is a cyclic convolution operator acting on the bands, and $\mathbf{S} \in \mathbb{R}^{N_h^2 \times N^2}$ is a downsampling operator (satisfying the condition $\mathbf{S}\mathbf{S}^T = \mathbf{I}_{N_h^2}$);
3) $\mathbf{H}_m \in \mathbb{R}^{n_m \times N^2 L_m}$ and $\mathbf{H}_h \in \mathbb{R}^{n_h \times N_h^2 L}$ are the sensing matrices for the MS and HS images, with n_m and n_h the number of measurements used to sense the MS and HS images. A more detailed description of the structure of the sensing matrices will be presented later;
4) $\mathbf{N}_m \in \mathbb{R}^{n_m}, \mathbf{N}_h \in \mathbb{R}^{n_h}$ are additive noise terms; and
5) $\mathbf{y}_m \in \mathbb{R}^{n_m}$ and $\mathbf{y}_h \in \mathbb{R}^{n_h}$ are the observed MS and HS compressed images, respectively.

The image restoration problem considered in this paper consists on estimating the HR image $\mathbf{f}$ from the observed compressed measurements $\mathbf{y}_m$ and $\mathbf{y}_h$.

B. Problem Formulation

Based on the previous models (1), we propose to consider the following optimization problem in order to estimate the matrix $\mathbf{M}$ and the vector $\boldsymbol{\alpha}$ from the observed compressive images $\mathbf{y}_m$ and $\mathbf{y}_h$

$$\begin{aligned} &\underset{\mathbf{M},\boldsymbol{\alpha}}{\operatorname{argmin}}\ c(\mathbf{M},\boldsymbol{\alpha}) = f(\mathbf{M},\boldsymbol{\alpha}) + \nu\varphi(\boldsymbol{\alpha}) \\ &\text{s.t. } \boldsymbol{\alpha} \geq 0, \quad \mathbf{1}_p^T\mathbf{A} = \mathbf{1}_{N^2}^T,\ 0 \leq \mathbf{M} \leq 1 \end{aligned} \tag{2}$$

where $\geq$ means "elementwise greater than," $\mathbf{1}_p$ is an all ones $p \times 1$ vector and

$$f(\mathbf{M},\boldsymbol{\alpha}) = \frac{1}{2}\|\mathbf{y}_m - \mathbf{H}_m\mathbf{R}_\lambda\overline{\mathbf{M}}\boldsymbol{\alpha}\|_2^2 + \frac{1}{2}\|\mathbf{y}_h - \mathbf{H}_h\mathbf{S}_\mathbf{s}\overline{\mathbf{M}}\boldsymbol{\alpha}\|_2^2$$

includes two data fidelity terms related to the MS and HS images. Finally

$$\varphi(\boldsymbol{\alpha}) = \beta\|\mathbf{G}\boldsymbol{\alpha}\|_1 + (1-\beta)\|\mathbf{D}\boldsymbol{\alpha}\|_1 \tag{3}$$

is a regularization operator, where the first term enforces sparsity of abundance maps in a wavelet representation and the second one includes a form of total variation (TV) regularizer preserving sharp edges or object boundaries [32]. The construction of the dictionary $\mathbf{G}$ and the matrix $\mathbf{D}$ will be detailed in the section devoted to numerical experiments. Note that $\|\cdot\|_2$ and $\|\cdot\|_1$ are used for the l_2- and l_1- norms, and that ν and β are the regularization parameters. Note also that the constraints for α in (2) are the abundance nonnegativity constraint and the abundance sum-to-one constraint, which are classically used in HS imaging [27]. Moreover, the constraint for the matrix $\mathbf{M}$ expresses the fact that each spectral signature represents the reflectances of different materials that belong to the interval $[0, 1]$. Finally, note that including different weights for the two data fidelity terms as in [14] would be possible with the proposed approach. Including different weights in the fusion algorithm might be interesting when the noises associated with the HS and MS sensors have different variances.

III. Compressive Spectral Imagers

This section summarizes the principles behind two representative CSI devices considered in this paper, i.e., C-CASSI and SSCSI. Note that these two architectures have been implemented in practical applications (based on spatial and spectral coding), which explains why they have been considered in our work [33], [34]. Even though only two CSI devices are considered, the techniques developed here might be extended to other architectures such as those studied in [9], [10], [26]. Note that the structure of the matrix $\mathbf{H}$ is related to the optical architecture of each implementation. Finally, it is worth noting that the matrices $\mathbf{H}_m$ and $\mathbf{H}_h$ are instances of the matrices $\mathbf{H}$ presented in this section.

A. Colored CASSI

The CASSI is one of the most representative CSI architectures, which comprises a dispersive element and a coded aperture [33]. The coded aperture is the spatial coding optical element defined as a block-unblock lithographic mask or a spatial light modulator [11]. The CASSI architecture encodes the 3D data only in the spatial domain, i.e., each pixel of the coded aperture blocks or let pass the entire spectral information. The C-CASSI is a different variation of the CASSI system, which replaces the binary masks by multiple-patterned arrays of selectable optical filters or colored coded apertures to provide a richer modulation in both spatial and spectral domains [22]. C-CASSI reduces the number of 2-D measurements required to recover the underlying image due to the higher randomness of these 3-D coded aperture structures. Note that the coded source is dispersed by a prism and that the coded and dispersed source is captured by a focal plane array. The sensing representation of the C-CASSI system is depicted in Fig. 1. The ℓth snapshot intensity at the (i, j)th pixel of the detector using a colored coded aperture $\mathbf{T}^\ell$ is

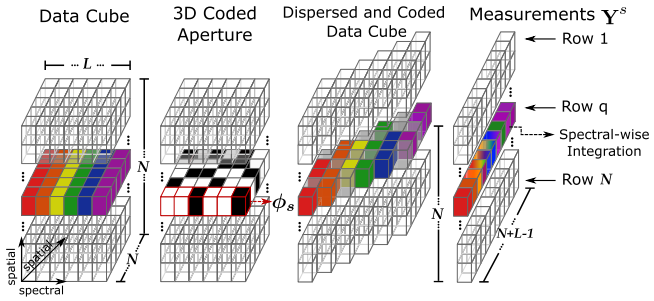

Fig. 1. Representation of the sensing phenomena behind CASSI system.

$$Y_{ij}^\ell = \sum_{k=0}^{L-1} \mathcal{F}_{i(j-k)k} T_{i(j-k)k}^\ell + \omega_{ij} \tag{4}$$

where $\boldsymbol{\mathcal{F}}$ is an $N \times N \times L$ spectral data cube, $T_{ijk}^\ell \in \{0, 1\}$ is the discretization of the ℓth colored coded aperture, ω_{ij} is the white Gaussian noise of the sensing system, and $\ell = 0, \ldots, K-1$ with $K \in \mathbb{N}$ representing the number of snapshots. All along the paper, the word "snapshot" refers to the energy captured by the 2-D sensor in a given integration time. Vectorizing the measurements $\mathbf{Y}_{ij}^\ell$ leads to

$$\mathbf{y}_\ell = \mathbf{H}_\ell\mathbf{f} + \boldsymbol{\omega} \tag{5}$$

where $\mathbf{y}_\ell \in \mathbb{R}^V$ is a vector representation of $\mathbf{Y}_{ij}^\ell$ with $V = N(N+L-1)$, $\mathbf{f} = \text{vec}([\mathbf{f}_0, \ldots, \mathbf{f}_{L-1}])$ is the vector representation of the data cube $\boldsymbol{\mathcal{F}}$, $\mathbf{f}_k$ is the vectorization of the k-th spectral band, and $\mathbf{H}_\ell \in \mathbb{R}^{V \times N^2 L}$ is the sensing matrix of the ℓth snapshot. The set of measurements associated with the K snapshots can be written as

$$\mathbf{y} = \mathbf{H}\mathbf{f} + \boldsymbol{\omega} \tag{6}$$

where $\mathbf{y} = [\mathbf{y}_0^T, \ldots, \mathbf{y}_{K-1}^T]^T$ contains all the measurements and $\mathbf{H} = [\mathbf{H}_0^T, \ldots, \mathbf{H}_{K-1}^T]^T \in \mathbb{R}^{KV \times N^2 L}$. An example of matrix $\mathbf{H}$ for $L = 3$ and $K = 2$ is displayed in Fig. 2. Note that the nonzero entries (indicated by white squares) of this matrix are determined by the 3-D color coded aperture. More precisely, the structure of the matrix $\mathbf{H}_\ell$ consists of a set of diagonal patterns determined by the ℓth colored coded aperture $\mathbf{T}^\ell$, which are located along the horizontal direction, such that one spatial dimension is shifted downward, as many times as

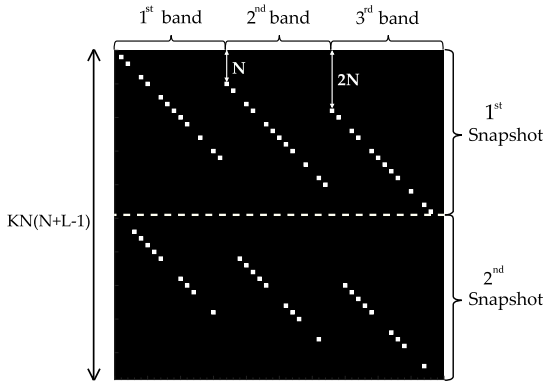

Fig. 2. Sensing matrix $\mathbf{H}$ of the CASSI architecture for $L = 3$ and $K = 2$. The white squares represent the passing (unblocking) elements.

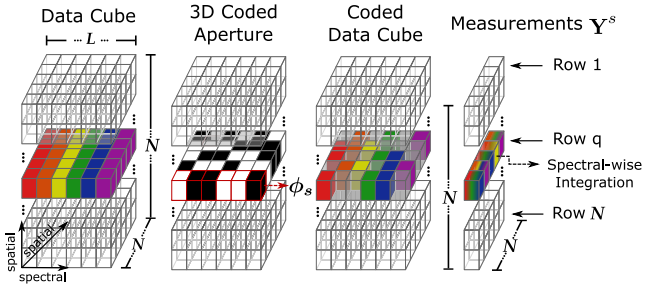

Fig. 3. Representation of the sensing phenomena behind SSCSI system.

the number of spectral bands. Finally, note that the structure of $\mathbf{H}$ is obtained by stacking the K matrices $\mathbf{H}_\ell$.

B. Spatio–Spectral Coded Compressive Spectral Imager SSCSI

Similar to C-CASSI, SSCSI optically modulates the 3-D data cube in both spatial and spectral dimensions, and acquires 2-D projections. The SSCSI proposed in [23] uses a diffraction grating to disperse the light into the spectrum plane and inserts a coding mask between the spectrum plane and the sensor plane to achieve the desired spatial–spectral modulation. A representation of the compression procedure behind SSCSI is shown in Fig. 3. The intensity of the ℓth snapshot at the (i, j)th pixel of the SSCSI detector is

$$Y_{ij}^{\ell} = \sum_{k=0}^{L-1} \mathcal{F}_{ijk} T_{ijk}^{\ell} + \omega_{ij}. \tag{7}$$

Note that SSCSI measurements are also defined as in (5) and (6) with $V = N^2$. However, the structure of the matrix $\mathbf{H}$ slightly differs from the one used in C-CASSI. It is also structured as a set of diagonal patterns without the downward shifting. Moreover, the patterns do not repeat horizontally, allowing spectral coding as shown in Fig. 4.

IV. Optimization Method

This section studies the optimization algorithm that is proposed to solve (2). Note that this problem is nonconvex

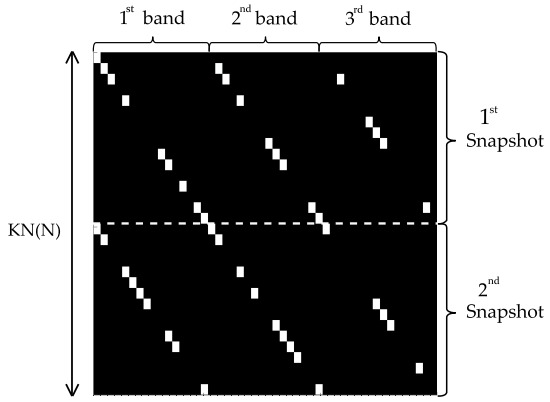

Fig. 4. Example of sensing matrix $\mathbf{H}$ in the SSCSI architecture for $L = 3$ and $K = 1$. White squares are used for ones (unblocking light).

with respect to $(\mathbf{M}, \boldsymbol{\alpha})$ [35], making its resolution challenging. The strategy investigated here is a block coordinate descent (BCD) approach, alternating optimizations with respect to the matrix $\mathbf{M}$ and the vector $\boldsymbol{\alpha}$ [35]. The two resulting optimization problems are convex and can thus be solved using the ADMM algorithm [36]. A sketch of the proposed strategy is detailed in Algorithm 1. The initialization of the algorithm and the optimization steps with respect to $\boldsymbol{\alpha}$ and $\mathbf{M}$ are detailed in the following sections.

Algorithm 1 Proposed Compressive Image Fusion

Input : $\mathbf{y}_m$,$\mathbf{y}_h$,$\mathbf{R}$, $\mathbf{B}$, $\mathbf{S}$, $\mathbf{H}_m$, $\mathbf{H}_h$
Output: $\boldsymbol{\alpha}^{(\mathbf{t})}$ and $\mathbf{M}^{(t)}$
1: $\mathbf{M}^{(0)} = \mathrm{EE}(\mathbf{y}_h)$ `%Endmember Extraction`
2: **for** $t = 1$ to stopping rule **do**
3: $\quad \boldsymbol{\alpha}^{(t)} = \underset{\boldsymbol{\alpha}\in\mathcal{A}}{\operatorname{argmin}} f(\mathbf{M}^{(t-1)}, \boldsymbol{\alpha}) + \varphi(\boldsymbol{\alpha})$ `% AL 2`
4: $\quad \mathbf{M}^{(t)} = \underset{\mathbf{M}\in\mathcal{M}}{\operatorname{argmin}} f(\mathbf{M}, \boldsymbol{\alpha}^{(t)})$ `% AL 3`
5: **end for**

A. Initialization

The endmember matrix is initialized with a fast estimation approach based on the Rayleigh–Ritz (RR) theory [37]. The idea of this method is to estimate the signal subspace from the compressive measurements using the RR theory and to estimate the endmembers using the fact that the LMM constrains the endmembers to be located at the vertices of a simplex. More precisely, this approach first estimates a subset of eigenvectors to approximate the signal subspace via RR theory, and then searches the endmembers in the approximated subspace using the VCA [37].

B. Optimization With Respect to the Abundance Matrix $\boldsymbol{\alpha}$

The first step of the minimization problem (2) optimizes the cost function with respect to $\boldsymbol{\alpha}$ for a fixed $\mathbf{M}$ using the ADMM algorithm. An auxiliary variable is introduced to split

the objective function and the constraints leading to

$$\begin{aligned}\underset{\boldsymbol{\alpha},\mathbf{v}_i}{\operatorname{argmin}}\ & \frac{1}{2}\|\mathbf{y}_m - \mathbf{H}_m\mathbf{v}_1\|_2^2 + \frac{1}{2}\|\mathbf{y}_h - \mathbf{H}_h\mathbf{S}_d\mathbf{v}_3\|_2^2 \\ & + \lambda\|\mathbf{v}_5\|_1 + \lambda_{TV}\|\mathbf{v}_6\|_1 + i_{\mathcal{A}}(\mathbf{v}_7) \\ \text{s.t.}\ \ & \mathbf{v}_1 = \mathbf{R}_\lambda\overline{\mathbf{M}}\mathbf{v}_2 \quad \mathbf{v}_5 = \mathbf{G}\boldsymbol{\alpha} \\ & \mathbf{v}_2 = \boldsymbol{\alpha} \quad \mathbf{v}_6 = \mathbf{D}\boldsymbol{\alpha} \\ & \mathbf{v}_3 = \overline{\mathbf{M}}\mathbf{v}_4 \quad \mathbf{v}_7 = \boldsymbol{\alpha} \\ & \mathbf{v}_4 = \mathbf{B}_s\boldsymbol{\alpha} \end{aligned} \tag{8}$$

where $i = 1, \ldots, 7$, $\mathbf{S}_d = \mathbf{I}_L \otimes \mathbf{S}$, $\mathbf{B}_s = \mathbf{I}_p \otimes \mathbf{B}$, and the function $i_{\mathcal{A}}$ is defined on the set $\mathcal{A} = \{\boldsymbol{\alpha}|\boldsymbol{\alpha} \geq 0\}$ by

$$i_{\mathcal{A}}(\boldsymbol{\alpha}) = \begin{cases} 0, & \text{if } \boldsymbol{\alpha} \in \mathcal{A} \\ \infty, & \text{if } \boldsymbol{\alpha} \notin \mathcal{A}. \end{cases} \tag{9}$$

Note that the number of splitting variables could have been reduced, e.g., by eliminating $\mathbf{v}_2$. However, the proposed algorithm separates the spatial and spectral operations leading to subproblems which are simpler to solve. For convenience, we introduce the following notations:

$$\mathbf{v} = \begin{bmatrix} \mathbf{v}_1 \\ \mathbf{v}_2 \\ \mathbf{v}_3 \\ \mathbf{v}_4 \\ \mathbf{v}_5 \\ \mathbf{v}_6 \\ \mathbf{v}_7 \end{bmatrix}, \quad \mathbf{C} = \begin{bmatrix} \mathbf{0} \\ \mathbf{I} \\ \mathbf{0} \\ \mathbf{B}_s \\ \mathbf{G} \\ \mathbf{D} \\ \mathbf{I} \end{bmatrix}$$

$$\mathbf{E} = \begin{bmatrix} \mathbf{I} & -\mathbf{R}_\lambda\overline{\mathbf{M}} & \mathbf{0} & \mathbf{0} & \mathbf{0} & \mathbf{0} & \mathbf{0} \\ \mathbf{0} & \mathbf{I} & \mathbf{0} & \mathbf{0} & \mathbf{0} & \mathbf{0} & \mathbf{0} \\ \mathbf{0} & \mathbf{0} & \mathbf{I} & -\overline{\mathbf{M}} & \mathbf{0} & \mathbf{0} & \mathbf{0} \\ \mathbf{0} & \mathbf{0} & \mathbf{0} & \mathbf{I} & \mathbf{0} & \mathbf{0} & \mathbf{0} \\ \mathbf{0} & \mathbf{0} & \mathbf{0} & \mathbf{0} & \mathbf{I} & \mathbf{0} & \mathbf{0} \\ \mathbf{0} & \mathbf{0} & \mathbf{0} & \mathbf{0} & \mathbf{0} & \mathbf{I} & \mathbf{0} \\ \mathbf{0} & \mathbf{0} & \mathbf{0} & \mathbf{0} & \mathbf{0} & \mathbf{0} & \mathbf{I} \end{bmatrix}$$

and the cost function

$$\begin{aligned} h(\mathbf{v}) = \frac{1}{2}\|\mathbf{y}_m - \mathbf{H}_m\mathbf{v}_1\|_2^2 + \frac{1}{2}\|\mathbf{y}_h - \mathbf{H}_h\mathbf{S}_d\mathbf{v}_3\|_2^2 \\ + \lambda\|\mathbf{v}_5\|_1 + \lambda_{\text{TV}}\|\mathbf{v}_6\|_1 + i_{\mathcal{A}}(\mathbf{v}_7) \end{aligned}$$

with $\mathbf{E}\mathbf{v} = \mathbf{C}\boldsymbol{\alpha}$. Using these notations, (8) reduces to

$$\underset{\boldsymbol{\alpha},\mathbf{v}}{\operatorname{argmin}}\ h(\mathbf{v}) \quad \text{s.t. } \mathbf{E}\mathbf{v} = \mathbf{C}\boldsymbol{\alpha}. \tag{10}$$

The augmented Lagrangian associated with (10) is

$$\mathcal{L}(\boldsymbol{\alpha}, \mathbf{v}, \mathbf{g}) = h(\mathbf{v}) + \frac{\rho}{2}\|\mathbf{E}\mathbf{v} - \mathbf{C}\boldsymbol{\alpha} + \mathbf{g}\|_2^2, \tag{11}$$

where $\mathbf{g}$ is the scaled dual variable and $\rho \geq 0$ is weighting the augmented Lagrangian term. The exact procedure used for estimating $\boldsymbol{\alpha}$ is summarized in Algorithm 2, whereas more details are available in the separated technical report [38]. The total complexity of the Algorithm 2 is dominated by the update steps of $\mathbf{v}_1$ and $\mathbf{v}_3$ being $\mathcal{O}(K_h N_h(N_h + L - 1) + K_m N(N + L_m - 1))$ for C-CASSI and $\mathcal{O}(K_h N_h^2 + K_m N^2)$ for SSCSI.

Algorithm 2 ADMM Algorithm to Estimate $\boldsymbol{\alpha}$

Input : $\mathbf{y}_m$,$\mathbf{y}_h$,$\mathbf{R}$, $\mathbf{B}$, $\mathbf{S}$, $\mathbf{H}_m$, $\mathbf{H}_h$, $\mathbf{M}$, $\rho \geq 0$
Output: $\boldsymbol{\alpha}^{(k+1)}$
1: $\mathbf{v}^{(0)}, \mathbf{g}^{(0)}$
2: **for** $k = 1$ to stopping rule **do**
3: $\quad \boldsymbol{\alpha}^{(k+1)} = \underset{\boldsymbol{\alpha}}{\operatorname{argmin}}\ \mathcal{L}(\boldsymbol{\alpha}, \mathbf{v}^{(k)}, \mathbf{g}^{(k)})$
4: $\quad \mathbf{v}^{(k+1)} = \underset{\mathbf{v}}{\operatorname{argmin}}\ \mathcal{L}(\boldsymbol{\alpha}^{(k+1)}, \mathbf{v}, \mathbf{g}^{(k)})$
5: $\quad \mathbf{g}^{(k+1)} = \mathbf{g}^{(k)} + \mathbf{v}^{(k+1)} - \mathbf{C}\boldsymbol{\alpha}^{(k+1)}$
6: **end for**

Convergence: In order to guarantee the convergence of Algorithm 2, we need to ensure that the augmented Lagrangian in (11) is a proper convex and closed function, according to the ADMM algorithm. This condition is satisfied since (11) is the sum of nonnegative convex functions [36]. Moreover, since the proper convex optimization function is continuous, it is closed, ensuring the convergence of Algorithm 2 [39].

C. Optimization With Respect to the Endmember Matrix $\mathbf{M}$

The optimization of the cost function (2) with respect to $\mathbf{M}$ for a fixed $\boldsymbol{\alpha}$ can be solved by using the ADMM algorithm. To facilitate the solution of this problem, we first rewrite the HS image as $\mathbf{f} = \overline{\mathbf{A}}\mathbf{m}$, where $\mathbf{m} = \text{vec}(\mathbf{M}^T)$, $\overline{\mathbf{A}} = \mathbf{I}_L \otimes \mathbf{A}^T$, and $\mathbf{A} = [\boldsymbol{\alpha}_1, \ldots, \boldsymbol{\alpha}_{N^2}]$ contains the abundances of all the image pixels. This reparameterization leads to

$$\underset{\mathbf{m}}{\operatorname{argmin}} \frac{1}{2}\|\mathbf{y}_m - \mathbf{H}_m\mathbf{R}_\lambda\overline{\mathbf{A}}\mathbf{m}\|_2^2 + \frac{1}{2}\|\mathbf{y}_h - \mathbf{H}_h\mathbf{S}_\mathbf{s}\overline{\mathbf{A}}\mathbf{m}\|_2^2 + i_{\mathcal{M}}(\mathbf{m}) \tag{12}$$

where the function $i_{\mathcal{M}}(\mathbf{m})$ is a function defined in the set $\mathcal{M} = \{\mathbf{m}|0 \leq \mathbf{m} \leq 1\}$ as in (9). To solve this problem, we split the vector $\mathbf{m}$ into three auxiliary variables $\mathbf{w}_1$, $\mathbf{w}_2$, $\mathbf{w}_3$ in order to obtain the following problem

$$\begin{aligned} \underset{\mathbf{m},\mathbf{w}_i}{\operatorname{argmin}}\ & \frac{1}{2}\|\mathbf{y}_m - \mathbf{H}_m\mathbf{w}_1\|_2^2 + \frac{1}{2}\|\mathbf{y}_h - \mathbf{H}_h\mathbf{S}_d\mathbf{w}_2\|_2^2 + i_{\mathcal{M}}(\mathbf{w}_3) \\ \text{s.t. } & \mathbf{w}_1 = \mathbf{R}_\lambda\overline{\mathbf{A}}\mathbf{m}, \quad \mathbf{w}_3 = \mathbf{m}, \ \mathbf{w}_2 = \hat{\mathbf{A}}\mathbf{m}. \end{aligned} \tag{13}$$

where $j = 1, \ldots, 3$, and $\hat{\mathbf{A}} = \mathbf{I}_L \otimes \mathbf{B}\mathbf{A}$. For notational convenience, we introduce the following quantities:

$$\mathbf{w} = \begin{bmatrix} \mathbf{w}_1 \\ \mathbf{w}_2 \\ \mathbf{w}_3 \end{bmatrix}, \quad \mathbf{E} = \begin{bmatrix} \mathbf{R}_\lambda\overline{\mathbf{A}} \\ \hat{\mathbf{A}} \\ \mathbf{I} \end{bmatrix}$$

and the cost function

$$l(\mathbf{w}) = \frac{1}{2}\|\mathbf{y}_m - \mathbf{H}_m\mathbf{R}_\lambda\mathbf{w}_1\|_2^2 + \frac{1}{2}\|\mathbf{y}_h - \mathbf{H}_h\mathbf{S}_d\mathbf{w}_2\|_2^2 + g(\mathbf{w}_3).$$

As a consequence, (13) reduces to

$$\underset{\mathbf{m},\mathbf{w}}{\operatorname{argmin}}\ l(\mathbf{w}) \quad \text{s.t. } \mathbf{w} = \mathbf{E}\mathbf{m} \tag{14}$$

with the following augmented Lagrangian:

$$\mathcal{L}(\mathbf{m}, \mathbf{w}, \mathbf{d}) = l(\mathbf{w}) + \frac{\rho}{2}\|\mathbf{w} - \mathbf{E}\mathbf{m} + \mathbf{d}\|_2^2 \tag{15}$$

where $\mathbf{d}$ is the scaled dual variables and $\rho \geq 0$ is weighting the augmented Lagrangian term. The ADMM algorithm for $\mathbf{m}$ is summarized in Algorithm 3 with more details in [38]. The complexity of Algorithm 3 is dominated by the update steps of $\mathbf{w}_1$ and $\mathbf{w}_2$ being $\mathcal{O}(K_h N_h (N_h + L - 1) + K_m N (N + L_m - 1))$ for C-CASSI and $\mathcal{O}(K_h N_h^2 + K_m N^2)$ for SSCSI.

Algorithm 3 ADMM Algorithm to Estimate $\mathbf{m}$

Input : $\mathbf{y}_m$,$\mathbf{y}_h$,$\mathbf{R}$, $\mathbf{B}$, $\mathbf{S}$, $\mathbf{H}_m$, $\mathbf{H}_h$, $\boldsymbol{\alpha}$, $\rho \geq 0$
Output: $\mathbf{m}^{(k+1)}$
1: $\mathbf{w}^{(0)}$, $\mathbf{d}^{(0)}$
2: **for** $k = 1$ to stopping rule **do**
3: $\quad \mathbf{m}^{(k+1)} = \underset{\mathbf{m}}{\operatorname{argmin}} \ \mathcal{L}(\mathbf{m}, \mathbf{w}^{(k)}, \mathbf{d}^{(k)})$
4: $\quad \mathbf{w}^{(k+1)} = \underset{\mathbf{w}}{\operatorname{argmin}} \ \mathcal{L}(\mathbf{m}^{(k+1)}, \mathbf{w}, \mathbf{d}^{(k)})$
5: $\quad \mathbf{d}^{(k+1)} = \mathbf{d}^{(k)} + \mathbf{w}^{(k+1)} - \mathbf{E}\mathbf{m}^{(k+1)}$
6: **end for**

Convergence: The energy function (15) is proper convex as the sum of nonnegative convex functions. Moreover, since the proper convex optimization function is continuous, it is closed guaranteeing the convergence of Algorithm 3 [39].

D. Global Algorithm Convergence

The optimization problem in (2) viewed as a function of $\boldsymbol{\alpha}$ for a given value of $\mathbf{M}$ (i.e., problem (8)) is convex. A similar comment can be made for problem (13), which optimizes the cost function with respect to $\mathbf{M}$ for a given value of $\boldsymbol{\alpha}$. The cost function c in (2) is continuous and has compact level sets. Moreover, the function f is differentiable ensuring that the function c is regular in the sense of [40]. As a consequence, from [40, Th. 4.1(b)], we know that every limit point of the sequence $\{\boldsymbol{\alpha}^{(t)}, \mathbf{M}^{(t)}\}$ generated by Algorithm 1 is a stationary point of the considered optimization problem. Finally, note that the BCD algorithm requires the exact solution of each subproblem and that these solutions are reached asymptotically with the ADMM algorithm.

V. Simulation Results

This section studies the fusion results for HS and MS compressed images obtained using the proposed algorithm for three different data sets with available ground truth. Following Wald's protocol [15], each reference image was degraded to generate the MS and HS images to be fused. The HS image was generated by applying a spatial blur to the reference image with a 7×7 Gaussian filter with standard deviation $\sigma = 1.5$ and by downsampling the result by a factor of 4 in each direction. The MS image was generated by uniformly downsampling the spectral dimension of the reference image resulting in an M-band MS image, with $\mathrm{M} \in \{6, 9, 10\}$, for data sets 1, 2, and 3, respectively. The observed HS and MS images were finally compressed using C-CASSI or SSCSI systems with sensing matrices whose nonzero entries were generated using a Bernoulli distribution. Indeed, the optical filters can be modeled as realizations of a Bernoulli random variable where the value "1" corresponds to a light-transmissive element and the value "0" to a blocking element [22], [24]. The compression ratio was fixed to 0.5. Except where it is mentioned, the HS and MS compressed images were both contaminated by the additive white Gaussian noise, with a signal to noise ratio equal to SNR = 30 dB for every snapshot.

TABLE I
Performance of MS + HS Fusion Methods (Jasper Data Set): PSNR (in Decibels), UIQI, SAM (in Degrees), ERGAS, DD ($\times 10^{-2}$), Time (in Seconds) and the Data (%)

Methods	PSNR	UIQI	SAM	ERGAS	DD	Time	Data
C-CASSI	39.75	**0.999**	**1.319**	**1.491**	0.492	**12.04**	**50%**
SSCSI	39.22	**0.999**	1.401	1.545	**0.436**	13.58	**50%**
[20]	31.55	0.995	3.103	1.665	1.949	15.75	**50%**
[21]	27.64	0.971	5.875	8.802	4.103	663.3	**50%**
FUMI	**39.76**	0.997	1.933	1.623	0.491	25.81	100%

Before running the proposed algorithm, we need to define the matrices $\mathbf{G}$, $\mathbf{D}$ and the different hyperparameters in (3). Following [22], the dictionary $\mathbf{G}$ was selected as the Kronecker product $\mathbf{I}_p \otimes \Psi$, where Ψ is a symmlet wavelet kernel. The operator $\mathbf{D}$ was decoupled in two operators acting on the rows and columns of each abundance map, as explained in [41]. The regularization hyperparameters ν and β were chosen by cross validation for each data set in order to obtain the best performance in terms of the PSNR metric (as classically done for this kind of problems).

The results obtained with the proposed fusion strategy are compared with the FUMI method of [18] (that does not use compressive measurements) and with the compressive fusion strategy proposed in [20] (that does not use spectral unmixing). We also consider the method studied in [21] for the first data set (Jasper).[1] Since the approach in [21] processes the images with the same spatial and spectral resolutions, we upsampled the HS image to the spatial resolution of the MS image and the MS image to the spectral resolution of the MS image by bicubic interpolation. The approach in [21] was then applied band per band to the two interpolated images.

A. Jasper Data Set

The Jasper Ridge HS image is of size $128 \times 128 \times 66$ [42], [43] and contains $p = 4$ endmembers. The quantitative fusion results are reported in Table I, whereas the qualitative fusion results are displayed in Figs. 5 and 6. The reader is invited to consult the references [13], [18], [20] for definitions of the metrics considered in the different tables. The reconstructed images using the proposed algorithm are displayed in Fig. 5(f) and (g). They are visually very close to the results obtained with FUMI, which is based on the full data set without CS. The FUMI method provides a reference in terms of PSNR, which is understandable since it processes images without CS, while the methods in [20] and [21] provide poor results. Fig. 6 displays examples of reconstructed pixel reflectances obtained with the proposed method that can be compared with the method in [29] and FUMI. The advantage

[1]The authors are very grateful to T. Wan and A. Achim for sharing their codes allowing a fair comparison.

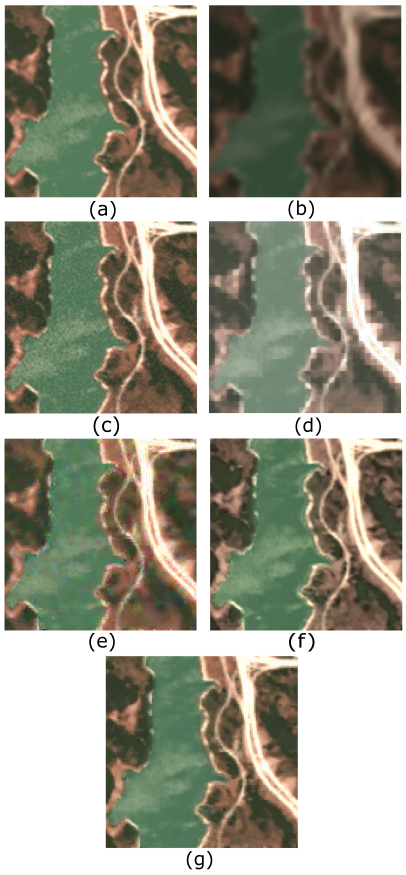

Fig. 5. Fusion results (Jasper data set): (a) MS image. (b) HS image. (c) FUMI (no compression). (d) [21]. (e) Method of [20] using the C-CASSI system. (f) Proposed method with 50% compression using the C-CASSI system. (g) Proposed method with 50% compression using the SSCSI system.

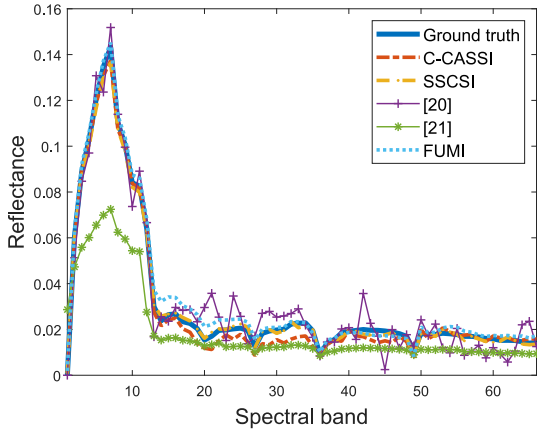

Fig. 6. Reconstructed reflectance of the pixel (54, 45) using the proposed approach, the methods of [20] and [21] and FUMI, compared to the Jasper ground truth.

of using the LMM can be clearly observed on this example since the reconstructed reflectance obtained with the method in [29] deviates more significantly from the ground truth. On the other hand, the numerical results illustrated in Table I indicate that the proposed method slightly outperforms FUMI even if it uses a reduced amount of data and requires less execution time.

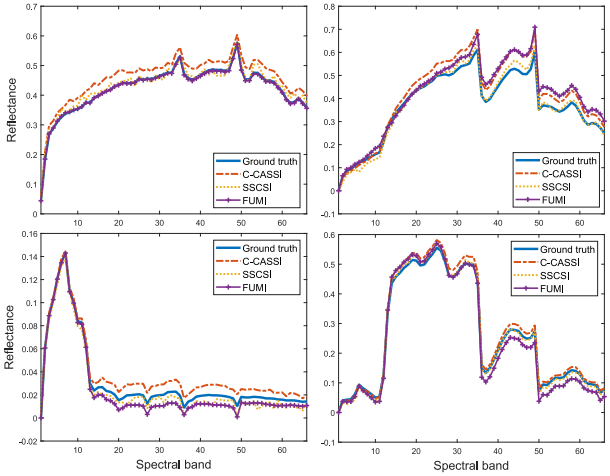

Fig. 7. Four unmixed endmembers for the Jasper data set obtained using FUMI and the proposed method with the C-CASSI and SSCSI systems, which are compared to the ground truth.

TABLE II

UNMIXING PERFORMANCE (JASPER DATA SET). SAM (IN DEGREES), NMSE_M (IN DECIBELS), AND NMSE_A (IN DECIBELS)

Methods	SAM_M	NMSE_M	NMSE_A
C-CASSI	**2.7075**	-20.3326	-14.834
SSCSI	2.7127	**-28.6689**	-13.646
FUMI	4.0634	-21.1070	**-18.579**

Since the proposed fusion method allows spectral unmixing, it is interesting to analyze the quality of the abundance and endmember estimates. The estimated endmembers are displayed in Fig. 7, whereas quantitative results related to unmixing are provided in Table II. The quality of the unmixing results is evaluated using the normalized mean square error of the abundance and endmember matrices (referred to as NMSE_A and NMSE_M). The spectral distortion of the endmembers is also computed using the spectral angle mapper (SAM) denoted as SAM_M [44]. These results show that the estimated endmembers are very close to the ground truth even if the fusion has been performed using images with a significantly reduced number of measurements. Table II confirms that the proposed method provides competitive quantitative results with respect to FUMI.

B. Urban Data Set

In this experiment, the reference image is a section of 256×256 pixels of the Urban HS image [42], [43], whose spectral dimension was subsampled by a factor of 2 resulting in a reference image of size $256 \times 256 \times 81$. The compressed images were both contaminated by additive white Gaussian noise, with a signal to noise ratio equal to $\text{SNR} = 30$ dB for the HS image and $\text{SNR} = 40$ dB for the MS image for every snapshot. The number of endmembers present in this scene is $p = 6$. Quantitative and qualitative fusion results are presented in Table III and in Figs. 8 and 9. Quantitative unmixing results are also reported in Table IV, whereas the estimated endmembers are shown in Fig. 10. Visual results in Fig. 8

TABLE III

PERFORMANCE OF MS + HS FUSION METHODS (URBAN DATA SET). PSNR (IN DECIBELS), UIQI, SAM (IN DEGREES), ERGAS, DD ($\times 10^{-2}$), TIME (IN SECONDS) AND THE DATA (%)

Methods	PSNR	UIQI	SAM	ERGAS	DD	Time	Data
C-CASSI	38.04	**0.997**	1.810	1.791	0.518	76.31	**50%**
SSCSI	37.46	**0.997**	1.969	1.935	**0.501**	90.78	**50%**
[20]	31.02	**0.977**	3.280	2.553	1.077	55.04	**50%**
FUMI	**38.82**	0.996	**1.554**	**0.940**	0.517	**46.31**	100%

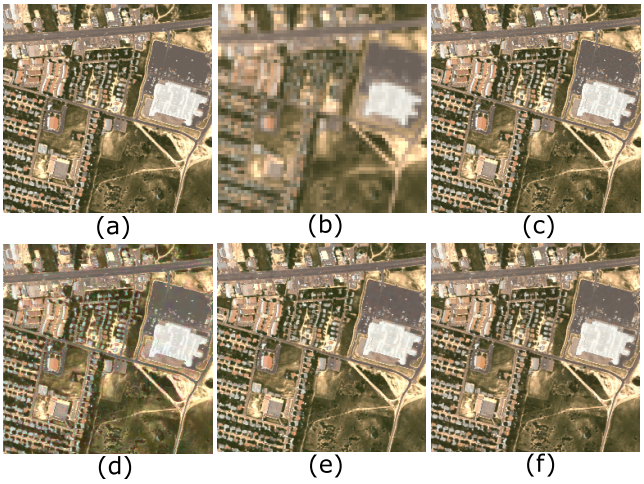

Fig. 8. Fusion results (Urban data set). (a) MS image. (b) HS image. (c) FUMI method without compression. (d) Method proposed in [20] using C-CASSI. (e) Proposed method with 50% compression using C-CASSI. (f) Proposed method with 50% compression using SSCSI.

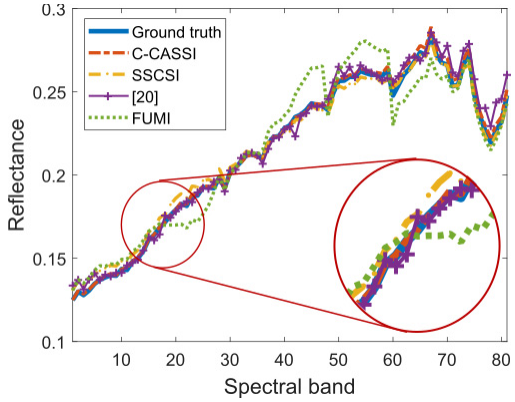

Fig. 9. Reflectance of the pixel $(45, 54)$ using the proposed approach, the method proposed in [20], and FUMI compared to the Urban ground truth.

show that the estimated image is very close to the ground truth. Figs. 9 and 10 show that the estimated signatures can follow the spectral variations of the ground truth. Moreover, quantitative results reported in Tables III and IV indicate that all performance measures used to evaluate the fusion and unmixing are very satisfactory even if the fusion has been performed using CS images with a significantly reduced number of measurements.

C. Pavia Data Set

The reference image used in this last experiment is the scene acquired over Pavia (Northern Italy) by the reflective optics

TABLE IV

UNMIXING PERFORMANCE (URBAN DATA SET). SAM (IN DEGREES), NMSE_M (IN DECIBELS), AND NMSE_A (IN DECIBELS)

Methods	SAM_M	NMSE_M	NMSE_A
C-CASSI	6.1867	-18.6986	-6.8705
SSCSI	**3.3516**	**-20.2430**	-7.3808
FUMI	6.8097	-19.7747	**-7.4057**

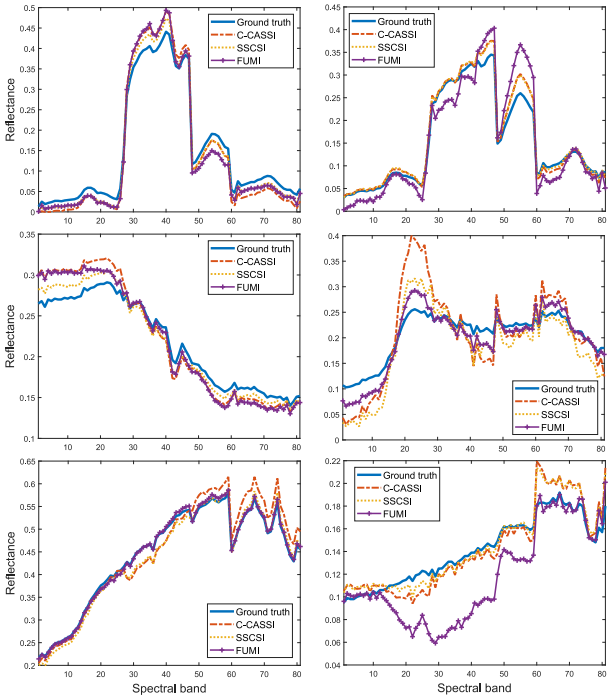

Fig. 10. Six unmixed endmembers for the Urban data set obtained using FUMI and the proposed method with C-CASSI and SSCSI systems with a comparison to the ground truth.

TABLE V

PERFORMANCE OF MS + HS FUSION METHODS (PAVIA DATA SET). PSNR (IN DECIBELS), UIQI, SAM (IN DEGREES), ERGAS, DD ($\times 10^{-2}$), TIME (IN SECONDS), AND THE DATA (%)

Methods	PSNR	UIQI	SAM	ERGAS	DD	Time	Data
C-CASSI	42.20	**0.996**	2.678	2.832	0.603	**18.23**	**50%**
SSCSI	41.59	0.995	2.807	3.151	0.709	22.49	**50%**
[20]	34.39	0.969	3.141	3.454	1.201	19.48	**50%**
FUMI	**43.34**	0.995	**2.216**	**1.395**	**0.573**	37.64	100%

system imaging spectrometer. We worked with a section of the image containing 128×128 pixels leading to a reference image of size $128 \times 128 \times 103$. Quantitative and qualitative fusion results are reported in Table V and Fig. 11. The results in Table V indicate that the proposed approach yields a competitive performance when compared to the FUMI method run on the full data set. The reader is invited to consult the technical report [38] for additional experiments associated with the full data set and with a more realistic simulation of the MS image.

D. Impact of the Compressive Ratio

The last experiments analyze the performance of the proposed algorithm for different numbers of measurements

Fig. 11. Fusion results (Pavia Data Set). (a) MS image. (b) HS image. (c) FUMI method with no compression. (d) Method proposed in [20] using C-CASSI. (e) Proposed method with 50% compression using C-CASSI. (f) Proposed method with 50% compression using SSCSI.

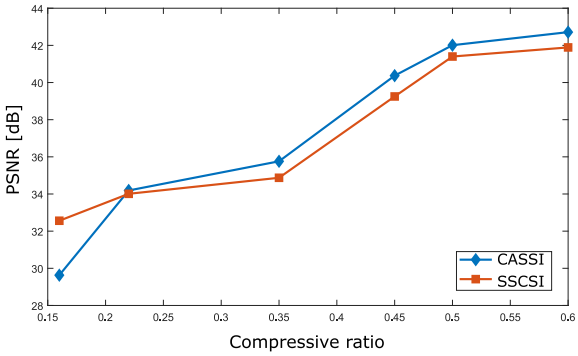

Fig. 12. PSNRs obtained with the proposed compressive fusion method for different amounts of data for CASSI and SSCSI systems.

extracted from the Pavia data set. The PSNRs of the reconstructed images for CASSI and SSCSI as function of the compressive ratio are depicted in Fig. 12. They indicate that the accuracy of the recovered images is directly proportional to the amount of data, as expected.

E. Sensitivity of the Algorithm to the Parameters ν and β

The performance of the proposed algorithm is sensitive to the values of the regularization parameters β and ν. In order to analyze this sensitivity, we varied the hyperparameters in appropriate intervals and evaluated the fusion results in terms of PSNR for all the parameter values. Fig. 13 displays the obtained PSNRs as functions of β and ν. As we can see, the parameter ν plays a dominant role in the proposed method since the results are less sensitive to the value of β.

VI. Algorithm Convergence

In order to illustrate the good convergence of Algorithm 1, a typical evolution of the cost function (2) as a function of the iteration number is displayed in Fig. 14. The Jasper data set was used for this experiment and the compressive measurements were simulated with the C-CASSI system with an SNR equal to 30 dB. Fig. 14 confirms the fast convergence of the algorithm to a critical point of the objective function,

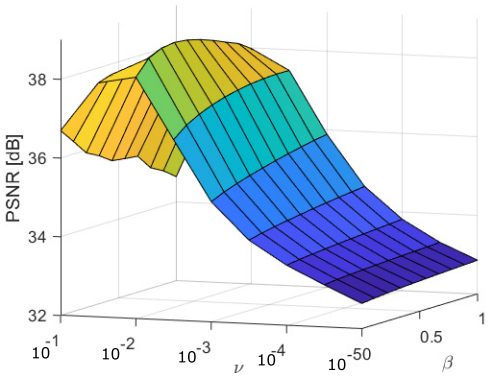

Fig. 13. Variations of PSNR as functions of parameters ν and β.

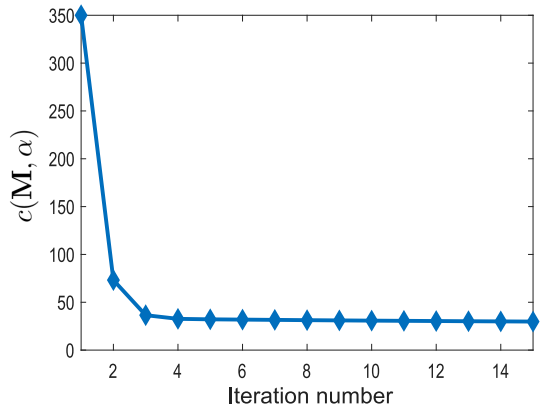

Fig. 14. Typical evolution of the objective function $c(\mathbf{M}, \alpha)$ defined in (2) during the optimization using Algorithm 1.

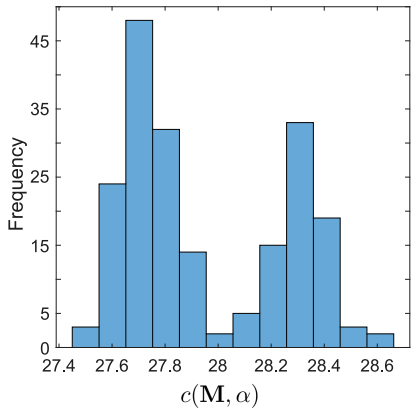

Fig. 15. Histogram of the final values of the objective function $c(\mathbf{M}, \alpha)$ in (2) obtained after 200 different endmember initializations.

which is here close to 27.73. Note that one iteration of Algorithm 1 includes one iteration of Algorithms 2 and 3. In order to analyze the sensitivity to initialization, we ran the proposed algorithm with 200 different initializations. These initializations were obtained by computing different noisy versions of the endmembers estimated with the method presented in [37]. More precisely, the endmembers resulting from [37] were corrupted by different white Gaussian noise sequences with the same SNR equal to 30 dB. The histogram of the corresponding values of the objective function is plotted in Fig. 15 showing two different modes, confirming the non-convexity of the fusion problem (2). Table VI shows the

TABLE VI

COMPARISON OF THE TWO MODES IN JASPER DATA SET. OBJECTIVE FUNCTION VALUE, PSNR (IN DECIBELS), UIQI, SAM (IN DEGREES), ERGAS, DD ($\times 10^{-2}$)

Obj	PSNR	UIQI	SAM	ERGAS	DD
27.727	38.6712	0.999	1.508	1.6634	0.474
28.196	39.6982	0.999	1.341	1.4779	0.426

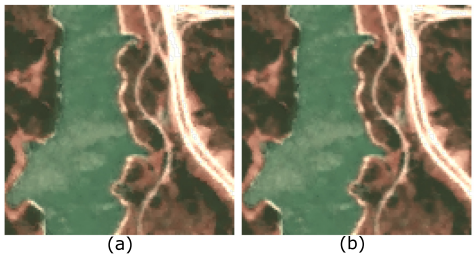

Fig. 16. Reconstructed images with two different values of the objective function, namely (a) $c(\mathbf{M}, \alpha) = 27.73$ and (b) $c(\mathbf{M}, \alpha) = 28.20$.

quantitative results associated with images corresponding to the two modes shown in Fig. 15, whereas reconstructed images corresponding to these two modes are displayed in Fig. 16. These results show that the reconstructed images are visually almost indistinguishable and that the quantitative results are very similar, confirming the good performance of the proposed fusion algorithm.

VII. CONCLUSION

This paper studied a new fusion algorithm based on spectral unmixing for reconstructing a high-spatial high-spectral image from two compressed MS and HS images. Our results showed that it is possible to recover an HR HS image from compressive spectral imagers, using fewer data samples than using conventional techniques. Future work includes the development of a new method for endmember extraction from compressed HS images to find a better initialization step for endmembers. Regularization parameters were estimated by cross validation in this paper. It would be also interesting to study methods allowing these parameters to be estimated directly from the data such as the methods investigated in [45].

REFERENCES

[1] S. M. Hsu and H.-H. K. Burke, "Multisensor fusion with hyperspectral imaging data: Detection and classification," *Lincoln Lab. J.*, vol. 14, no. 1, 2003.

[2] M. E. Schaepman, S. L. Ustin, A. J. Plaza, T. H. Painter, J. Verrelst, and S. Liang, "Earth system science related imaging spectroscopy—An assessment," *Remote Sens. Environ.*, vol. 113, pp. 123–137, Sep. 2009.

[3] S. V. Panasyuk *et al.*, "Medical hyperspectral imaging to facilitate residual tumor identification during surgery," *Cancer Biol. Therapy*, vol. 6, no. 3, pp. 439–446, 2007.

[4] N. F. Schreiber *et al.*, "The SINS survey: SINFONI integral field spectroscopy of $z\sim$ 2 star-forming galaxies," *Astrophys. J.*, vol. 706, no. 2, p. 1364, 2009.

[5] G. A. Shaw and H.-H. K. Burke, "Spectral imaging for remote sensing," *Lincoln Lab. J.*, vol. 14, no. 1, pp. 3–28, 2003.

[6] E. M. Middleton *et al.*, "The earth observing one (EO-1) satellite mission: Over a decade in space," *IEEE J. Sel. Topics Appl. Earth Observ. Remote Sens.*, vol. 6, no. 2, pp. 243–256, Apr. 2013.

[7] S. Foucart and H. Rauhut, *A Mathematical Introduction to Compressive Sensing*, vol. 1, no. 3. Basel, Switzerland: Birkhäuser, 2013.

[8] M. E. Gehm, R. John, D. J. Brady, R. M. Willett, and T. J. Schulz, "Single-shot compressive spectral imaging with a dual-disperser architecture," *Opt. Express*, vol. 15, no. 21, pp. 14013–14027, 2007.

[9] M. F. Duarte *et al.*, "Single-pixel imaging via compressive sampling," *IEEE Signal Process. Mag.*, vol. 25, no. 2, pp. 83–91, Mar. 2008.

[10] C. V. Correa, C. A. A. Hinojosa, G. R. Arce, and H. Arguello, "Multiple snapshot colored compressive spectral imager," *Opt. Eng.*, vol. 56, no. 4, p. 041309, 2016.

[11] G. R. Arce, D. J. Brady, L. Carin, H. Arguello, and D. S. Kittle, "Compressive coded aperture spectral imaging: An introduction," *IEEE Signal Process. Mag.*, vol. 31, no. 1, pp. 105–115, Jan. 2014.

[12] H. Arguello and G. R. Arce, "Spectrally selective compressive imaging by matrix system analysis," *Proc. Imag. Appl. Opt. Tech. Papers*, Washington, DC, USA: OSA, Jun. 2012.

[13] Q. Wei, J. Bioucas-Dias, N. Dobigeon, and J. Y. Tourneret, "Hyperspectral and multispectral image fusion based on a sparse representation," *IEEE Trans. Geosci. Remote Sens.*, vol. 53, no. 7, pp. 3658–3668, Jul. 2015.

[14] M. Simoes, J. Bioucas-Dias, L. B. Almeida, and J. Chanussot, "A convex formulation for hyperspectral image superresolution via subspace-based regularization," *IEEE Trans. Geosci. Remote Sens.*, vol. 53, no. 6, pp. 3373–3388, Jun. 2015.

[15] L. Loncan *et al.*, "Hyperspectral pansharpening: A review," *IEEE Trans. Geosci. Remote Sens.*, vol. 3, no. 3, pp. 27–46, Sep. 2015.

[16] G. Vivone *et al.*, "A critical comparison among pansharpening algorithms," *IEEE Trans. Geosci. Remote Sens.*, vol. 53, no. 5, pp. 2565–2586, May 2015.

[17] B. Zhukov, D. Oertel, F. Lanzl, and G. Reinhackel, "Unmixing-based multisensor multiresolution image fusion," *IEEE Trans. Geosci. Remote Sens.*, vol. 37, no. 3, pp. 1212–1226, May 1999.

[18] Q. Wei, J. Bioucas-Dias, N. Dobigeon, J.-Y. Tourneret, M. Chen, and S. Godsill, "Multiband image fusion based on spectral unmixing," *IEEE Trans. Geosci. Remote Sens.*, vol. 54, no. 12, pp. 7236–7249, Dec. 2016.

[19] N. Yokoya, T. Yairi, and A. Iwasaki, "Coupled nonnegative matrix factorization unmixing for hyperspectral and multispectral data fusion," *IEEE Trans. Geosci. Remote Sens.*, vol. 50, no. 2, pp. 528–537, Feb. 2012.

[20] E. Vargas, O. Espitia, H. Arguello, and J.-Y. Tourneret, "Spectral image fusion from compressive measurements," *IEEE Trans. Image Process.*, vol. 28, no. 5, pp. 2271–2282, May 2019.

[21] T. Wan, N. Canagarajah, and A. Achim, "Compressive image fusion," in *Proc. Int. Conf. Image Process. (ICIP)*, San Diego, CA, USA, Oct. 2008, pp. 1308–1311.

[22] H. Arguello and G. R. Arce, "Colored coded aperture design by concentration of measure in compressive spectral imaging," *IEEE Trans. Image Process.*, vol. 23, no. 4, pp. 1896–1908, Apr. 2014.

[23] X. Lin, Y. Liu, J. Wu, and Q. Dai, "Spatial-spectral encoded compressive hyperspectral imaging," *ACM Trans. Graph.*, vol. 33, no. 6, Nov. 2014, Art. no. 233.

[24] H. Rueda, H. Arguello, and G. R. Arce, "DMD-based implementation of patterned optical filter arrays for compressive spectral imaging," *J. Opt. Soc. Amer. A, Opt. Image Sci.*, vol. 32, no. 1, pp. 80–89, 2015.

[25] H. Arguello and G. R. Arce, "Rank minimization code aperture design for spectrally selective compressive imaging," *IEEE Trans. Image Process.*, vol. 22, no. 3, pp. 941–954, Mar. 2013.

[26] I. August, Y. Oiknine, M. AbuLeil, I. Abdulhalim, and A. Stern, "Miniature compressive ultra-spectral imaging system utilizing a single liquid crystal phase retarder," *Sci. Rep.*, vol. 6, Mar. 2016, Art. no. 23524.

[27] N. Keshava and J. F. Mustard, "Spectral unmixing," *IEEE Signal Process. Mag.*, vol. 19, no. 1, pp. 44–57, Jan. 2002.

[28] J. M. P. Nascimento and J. M. Bioucas-Dias, "Vertex component analysis: A fast algorithm to unmix hyperspectral data," *IEEE Trans. Geosci. Remote Sens.*, vol. 43, no. 4, pp. 898–910, Apr. 2005.

[29] T.-H. Chan, W.-K. Ma, A. Ambikapathi, and C.-Y. Chi, "A simplex volume maximization framework for hyperspectral endmember extraction," *IEEE Trans. Geosci. Remote Sens.*, vol. 49, no. 11, pp. 4177–4193, Nov. 2011.

[30] M. E. Winter, "N-FINDR: An algorithm for fast autonomous spectral end-member determination in hyperspectral data," *Proc. SPIE*, vol. 3753, pp. 266–275, Oct. 1999.

[31] Q. Wei, N. Dobigeon, and J. Y. Tourneret, "Bayesian fusion of multi-band images," *IEEE J. Sel. Topics Signal Process.*, vol. 9, no. 6, pp. 1117–1127, Sep. 2015.

[32] Y. Wang, J. Yang, W. Yin, and Y. Zhang, "A new alternating minimization algorithm for total variation image reconstruction," *SIAM J. Imag. Sci.*, vol. 1, no. 3, pp. 248–272, Aug. 2008.
[33] A. Wagadarikar, R. John, R. Willett, and D. Brady, "Single disperser design for coded aperture snapshot spectral imaging," *Appl. Opt.*, vol. 47, no. 10, pp. B44–B51, 2008.
[34] H. Arguello, H. Rueda, Y. Wu, D. W. Prather, and G. R. Arce, "Higher-order computational model for coded aperture spectral imaging," *Appl. Opt.*, vol. 52, no. 10, pp. D12–D21, 2013.
[35] D. P. Bertsekas, *Nonlinear Programming*. Belmont, MA, USA: Athena Scientific, 1999.
[36] S. Boyd, N. Parikh, E. Chu, B. Peleato, and J. Eckstein, "Distributed optimization and statistical learning via the alternating direction method of multipliers," *Found. Trends Mach. Learn.*, vol. 3, no. 1, pp. 1–122, Jan. 2011.
[37] E. Vargas, S. Pinilla, and H. Arguello, "A fast endmember estimation algorithm from compressive measurements," in *Proc. Eur. Signal Process. Conf. (EUSIPCO)*, Rome, Italy, Oct. 2018.
[38] E. Vargas, H. Arguello, and J.-Y. Tourneret, "Spectral image fusion from compressive measurements using spectral unmixing and a sparse representation of abundance maps," Univ. Toulouse, Toulouse, France, Tech. Rep., Jul. 2018. [Online]. Available: http://tourneret.perso.enseeiht.fr/publis_fichiers/technical_report_Fusion_Unmixing.pdf
[39] S. Boyd and L. Vandenberghe, *Convex Optimization*. Cambridge, U.K.: Cambridge Univ. Press, 2004.
[40] P. Tseng, "Convergence of a block coordinate descent method for nondifferentiable minimization," *J. Optim. Theory Appl.*, vol. 109, no. 3, pp. 475–494, 2001.
[41] A. Barbero and S. Sra. (Nov. 2014). "Modular proximal optimization for multidimensional total-variation regularization." [Online]. Available: https://arxiv.org/abs/1411.0589
[42] F. Zhu, Y. Wang, S. Xiang, B. Fan, and C. Pan, "Structured sparse method for hyperspectral unmixing," *ISPRS J. Photogramm. Remote Sens.*, vol. 88, pp. 101–118, Feb. 2014.
[43] F. Zhu, Y. Wang, B. Fan, S. Xiang, G. Meng, and C. Pan, "Spectral unmixing via data-guided sparsity," *IEEE Trans. Image Process.*, vol. 23, no. 12, pp. 5412–5427, Dec. 2014.
[44] P. E. Dennison, K. Q. Halligan, and D. A. Roberts, "A comparison of error metrics and constraints for multiple endmember spectral mixture analysis and spectral angle mapper," *Remote Sens. Environ.*, vol. 93, no. 3, pp. 359–367, 2004.
[45] M. Pereyra *et al.*, "Tutorial on stochastic simulation and optimization methods in signal processing," *IEEE J. Sel. Topics Signal Process.*, vol. 10, no. 2, pp. 224–241, Mar. 2016.

Edwin Vargas (S'18) received the B.S. and master's degrees in electronic engineering from the Universidad Industrial de Santander, Bucaramanga, Colombia, in 2016 and 2018, respectively, where he is currently pursuing the Ph.D. degree with the Department of the Electrical and Computer Engineering.

His research interests include high-dimensional signal processing, compressive sensing, and dictionary learning.

Henry Arguello (SM'11) received the master's degree in electrical engineering from the Universidad Industrial de Santander, Bucaramanga, Colombia, and the Ph.D. degree from the Electrical and Computer Engineering Department, University of Delaware, Newark, DE, USA.

He is currently a Titular Professor with the Systems Engineering Department, Universidad Industrial de Santander. His research interests include statistical signal processing, high-dimensional signal coding and processing, optical imaging, optical code design, and computational imaging.

Jean-Yves Tourneret (SM'08–F'19) received the Ingénieur degree in electrical engineering from the Ecole Nationale Supérieure d'Electronique, d'Electrotechnique, d'Informatique, d'Hydraulique et des Télécommunications (ENSEEIHT) de Toulouse, University of Toulouse, Toulouse, France, in 1989, and the Ph.D. degree from the National Polytechnic Institute of Toulouse, Toulouse, in 1992.

He is currently a Professor with the ENSEEIHT and a member of the IRIT Laboratory (UMR 5505 of the CNRS), University of Toulouse. His research interests include statistical signal and image processing with a particular interest to Bayesian and Markov chain Monte Carlo methods.

Dr. Tourneret was a member of different technical committees including the Signal Processing Theory and Methods committee of the IEEE Signal Processing Society from 2001 to 2007 and from 2010 to 2015, and the EURASIP SAT committee on Theoretical and Methodological Trends in Signal Processing. He served as the General Chair for the CIMI workshop on optimization and statistics in image processing hold in Toulouse in 2013 (with F. Malgouyres and D. Kouamé) and the International Workshop on Computational Advances in Multi-Sensor Adaptive Processing in 2015 (with P. Djuric) and in 2019 (with D. Brie). He has been serving as an Associate Editor for the IEEE TRANSACTIONS ON SIGNAL PROCESSING from 2008 to 2011 and since 2015, and the *EURASIP Journal on Signal Processing* since 2013.